

Heat conduction tuning by hyperbranched nanophononic metamaterials

Bing Li, K. T. Tan, and Johan Christensen

Citation: *Journal of Applied Physics* **123**, 205105 (2018); doi: 10.1063/1.5023487

View online: <https://doi.org/10.1063/1.5023487>

View Table of Contents: <http://aip.scitation.org/toc/jap/123/20>

Published by the [American Institute of Physics](#)

PHYSICS TODAY

WHITEPAPERS

MANAGER'S GUIDE

Accelerate R&D with
Multiphysics Simulation

READ NOW

PRESENTED BY
 COMSOL

Heat conduction tuning by hyperbranched nanophononic metamaterials

Bing Li,¹ K. T. Tan,^{1,a)} and Johan Christensen²

¹*Department of Mechanical Engineering, The University of Akron, Akron, Ohio 44325-3903, USA*

²*Universidad Carlos III de Madrid, ES-28916 Legans (Madrid), Spain*

(Received 24 January 2018; accepted 29 April 2018; published online 22 May 2018)

Phonon dispersion and thermal conduction properties of hyperbranched nanostructures with unique topological complexity are theoretically and numerically investigated in this research. We present analytical cantilever-in-mass models to analyze and control the inherent resonance hybridization in hyperbranched nanomembranes containing different configurations and cross sections. We show that these local resonances hosted by hyperbranched nanopillars can generate numerous flat bands in the phonon dispersion relation and dramatically lower the group velocities, consequently resulting in a significant reduction of the thermal conductivity. The applicability of the proposed analytical models in thermal conductivity tuning is demonstrated, and a superior performance in reducing the heat flux in nano-structured membranes is exhibited, which can potentially lead to improved thermoelectric energy conversion devices. *Published by AIP Publishing.*

<https://doi.org/10.1063/1.5023487>

I. INTRODUCTION

Driven by the promising performance in the flux manipulation of vibrational energy, phononic nanostructures have been regarded as candidates of enormous potential for many important applications in thermal engineering.¹ Several novel nanostructure-based thermal devices, such as thermal diodes,^{2,3} thermal cloaking,⁴ and heat imaging,⁵ have been reported to control heat transport. As a topic of particular recent interest, thermoelectric energy conversion has attracted increasing attention. Various man-made nanophononic structures have been investigated to target a remarkable reduction in thermal conductivity, while not hampering the properties of electronic transport, which plays a crucial role in achieving high heat-to-electricity conversion efficiency.⁶ Most of the common semiconductor nanostructures are able to reduce their thermal conductivity based on the design mechanisms of phonon scattering. By introducing more obstacles, such as impurity, interfaces, or periodic nanopores, the surface boundary and Bragg scattering are enhanced, leading to an observable reduction in thermal conductivity.^{7–10} However, along with a lower thermal conductivity, an undesirable blocking of the electron transport is likely to be induced simultaneously by the same scattering elements, which diminishes improvements to the figure of merit of thermoelectric energy conversion.^{11,12}

It is noted that the transmission of heat has the similar physical mechanism with the transmission of sound. Both can be managed by mechanical vibrations of the phonon atomic lattice.^{5,13} One difference is that large wavelengths correspond to sound wave oscillations, while short wavelengths correspond to heat oscillations. Analogous to the phononic crystals for sound control, in recent years, the phononic crystals with nanoscale periodicity have shown great potential for thermal flow control.^{5,13,14} Inspired by the creativity of electromagnetic/acoustic metamaterials,^{15–18} an

alternative strategy based on local phonon resonances has been recently presented for thermal conductivity modification, which is tailored in nanophononic metamaterials (NPMs).^{11,12,19} The concept of NPMs was proposed for the first time in a nanoscale configuration of pillared thin film.¹⁹ Resonance hybridizations between the local resonances of the periodic nanopillars and the bulk modes of the host membrane result in flattened bands in phonon dispersion relations, which directly alter the group velocities of phonons. Considering that heat is mostly carried by phonons in semi-conducting materials,²⁰ the modification can lead to a further reduction in thermal conductivity. Several pioneer studies have been conducted to evaluate the superior potential of branched NPM in heat conduction control by using lattice dynamics (LD) calculations,¹⁹ molecular dynamics (MD) simulations,^{11,21,22} and finite element analysis (FEA).^{23–26} It was further verified that the thermal conductivity reduction is induced by the local resonance of the nanopillars. A preliminary theoretical model was reported to analyze the flat hybridization bands and tailoring of the thermal conductivity in simple branched nanowires.²⁴ Parametric effects and a combination with the mechanisms of Bragg diffraction were also explored to optimize the thermodynamic properties of NPMs.^{11,23} The most recent experiment was presented to verify the change of thermal conductivity induced by the nanopillars.²⁷ It is possible that the branched nanopillars can potentially improve the figure of merit of thermoelectric materials and lower the thermal conductivity at low temperatures, while maintaining the high performance of electron transport.

Nevertheless, the research on locally resonant NPMs is still at the preliminary stage of development, and most of the proposed man-made NPMs are simple branched nanostructures. The mechanisms for the reduction of thermal conductivity in these structures are still diverging. Relevant experimental verification and theoretical investigation are scarce. In practice, the family of branched nanostructures

^{a)}Author to whom correspondence should be addressed: ktan@uakron.edu

appears to be very complex, and is based on a wide variety of configurations and non-uniform cross sections,^{28,29} such as dendritic and flowerlike nanowires/nanoplates.^{30–33} These hyperbranched nanostructures, with unique higher order topological complexity, can normally offer more functionalities due to their tunable physical/chemical properties, which are regarded as potential building blocks for future electronic, photonic and sensing nano-devices.³⁰ From the topological viewpoint, the design principle of complicated hyperbranched nanostructures is, to some extent, in accordance with the principle of locally resonant NPMs. Therefore, they are expected to have superior performance in phononic and thermoelectric nanodevices.

Considering that the local resonances of branched nanopillars play a critical role in thermal conductivity control and the cantilever-in-mass model is an effective approach to analyze the vibration characteristics of macroscopic mechanical metamaterial,³⁴ we further extended this model and theoretically investigated the phonon resonance hybridization in basic nanowires with only one simple nanopillar in the authors' previous work.²⁴ The branched nanopillar can be acted by a microcantilever in nanoscale and the host membrane can be described by a lumped mass. The phonon dispersion of the branched nanowire can be discussed by the cantilever-in-mass model. In addition, we can transform this cantilever-in-mass model into a classical lumped mass-spring model, which has been demonstrated as an efficient system to explore the unusual properties of elastic/mechanical metamaterials^{17,18,35} and has recently been extended to nanostructures.^{36,37} The equivalent mass-spring model can be applied to theoretically predict the resonance hybridization frequencies,²⁴ which are potentially significant for designing the branched nanomembrane and tailoring its thermal conductivity.

However, to the best of our knowledge, no analytical work has been reported about the heat conduction tuning using hyperbranched NPMs with higher-order topological complexity. This research gap in the literature is particularly stimulating since recent experiments are in good agreement with continuum modeling,²⁵ which in the long wavelength regime opens the possibility for analytical metamaterials treatment. In this work, for the first time, we systematically investigate the phonon resonance hybridization between complex hyperbranched nanopillars and the host nanomembrane. Based on the proposed cantilever-in-mass model, we develop various analytical models (mass-spring model, mass-in-mass

models with single/dual-resonator) to predict and control the flat bands in hyperbranched nanostructures with different orders of topological complexity. The influence of cross-sectional shape on the resonance hybridization is discussed. The effect of hyperbranched nanopillars on the modification of thermal conductivity is theoretically and numerically explored, and the superior performance of the proposed hyperbranched NPMs in heat conduction tuning is presented.

II. DESIGN AND RATIONALE

A. Modification of phonon dispersion

In this paper, we propose several different two-dimensional (2D) NPM structures to describe hyperbranched nanomembranes with various levels of topological complexity. An NPM membrane consisting of a basic branched unit cell (unit cell A) is sketched in Fig. 1(a), while the other higher-order hyperbranched unit cells (unit cells B and C) are depicted in Figs. 2(a) and 2(b), respectively. There is a basic nanopillar with a radius of R_1 in all unit cells. For unit cell B, an additional nanopillar with a different radius of R_2 is built on the opposite surface, while for unit cell C, an additional nanopillar resides on the side of the basic nanopillar to mimic a secondary growth. Without loss of generality, the additional nanopillar has different radius and length than the basic one. We design the two configurations of unit cells B and C on the basis of the basic growth approach for the fabrication of complicated hyperbranched nanostructures. Most of the reported synthetic techniques for a hyperbranched nanostructure with high order complexity are based on the secondary and tertiary growth of a host nanomembrane.^{30,31} For unit cells B and C, the fabrication process depends on the dimensions of the nanopillars. If the two nanopillars' dimensions are same or similar, it is possible to fabricate with configuration B by a secondary growth of the host nanomembrane. But for unit cell C, another tertiary growth is needed. If the two nanopillars' dimensions are different, both unit cells B and C will need a tertiary growth. It is expected that unit cell C enables an easier fabrication process because both nanopillars in this configuration are on the same surface side of the host membrane. In addition, the configuration unit cell C is more applicable for an extended growth than unit cell B where area is a limitation and there is only a restricted area on the host membrane. One potential extension of the hyperbranched nanostructure is a tree-like hyperbranched NPM, as shown in Fig. 2(c). Based on the

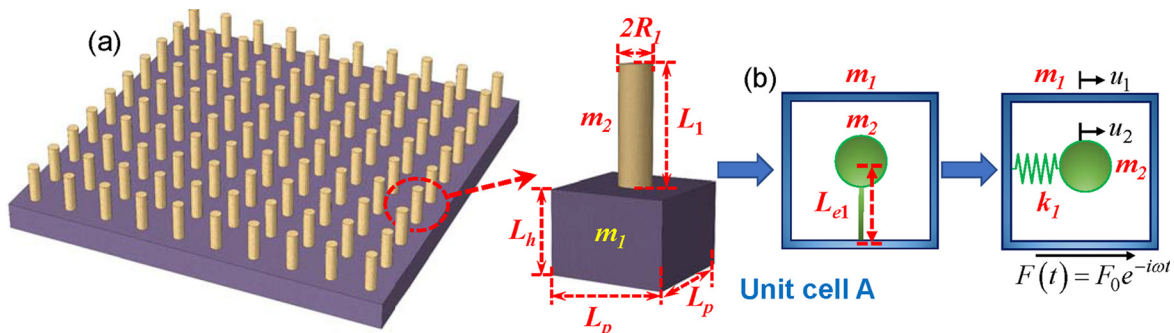


FIG. 1. (a) Sketch of an NPM membrane consisting of unit cell A and (b) the relevant cantilever-in-mass and mass-spring models.

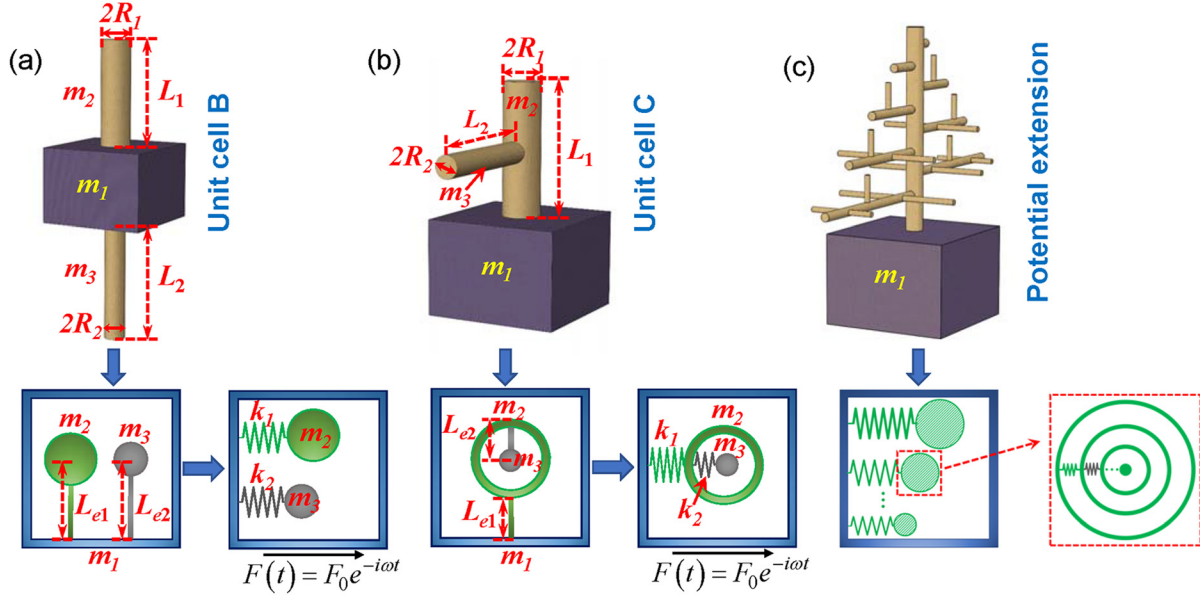


FIG. 2. Equivalent cantilever-in-mass and mass-spring models for hyperbranched NPM with (a) unit cell B and (b) unit cell C. (c) A potential extension of hyperbranched NPM.

investigation of heat conduction tuning by using unit cells B and C, we can propose applicable models for predicting the performance of a more complicated hyperbranched nanostructure, which is one potential benefit for practical applications.

We first investigate the effect of hyperbranched nanopillars on the phonon dispersion spectrums of a host nanomembrane using finite element analysis (FEA). A commercial FEA software, COMSOL Multiphysics, is selected to build the 3D continuum models for various unit cells. The arrangement of nanopillars is a periodic square lattice in the nanoscale. The material properties utilized in the FEA models are Young's modulus $E = 90$ GPa, Poisson's ratio $\nu = 0.26$, and density $\rho = 5600$ kg/m³. The dimensions of the nanopillars and host membrane in each unit cell [see Figs. 1(a) and 2] are $L_p = 60$ nm, $L_h = 50$ nm, $L_1 = 60$ nm, $R_1 = 8.46$ nm, and for unit cell B $L_2 = 65$ nm, $R_2 = 3R_1/5$; for unit cell C $L_2 = 70$ nm, $R_2 = R_1/2$. It should be mentioned that the FEA model used here is valid only for elastic surface scattering, which might be the case at low temperatures, but not for the case at room temperature, at which the scattering is mostly diffused, and thus local resonances cannot be formed.

According to the realistic size of the nanostructures, the eigenfrequencies from 0 to 100 GHz are calculated and the dispersion spectrum (0–30 GHz) is taken as an example. The considered frequency range is sufficient to evaluate thermal properties at 0.3 K.

In Fig. 3, we predict that the periodic hyperbranched nanopillars modify the original phonon spectrum of the host membrane, resulting in a series of flat hybridization bands in the dispersion relations being plotted. Compared to the dispersion spectrum obtained by the basic unit cell A [see Fig. 3(b)], the hyperbranched unit cells B and C successfully generate more flat hybridization bands [see Figs. 3(c) and 3(d)]. But the frequencies of these hybridization bands are different. It is clearly shown in Fig. 3 that more than twice the amount of flat bands are obtained by using the unit cells B and C as compared to unit cell A within the same frequency range, and the flatness of the band remains virtually unchanged with parallel momentum. As we will see later, the flattening of the branches of the phonon dispersion can directly reduce the group velocity, and will therefore modify the thermal conductivity. Consequently, increasing the flat

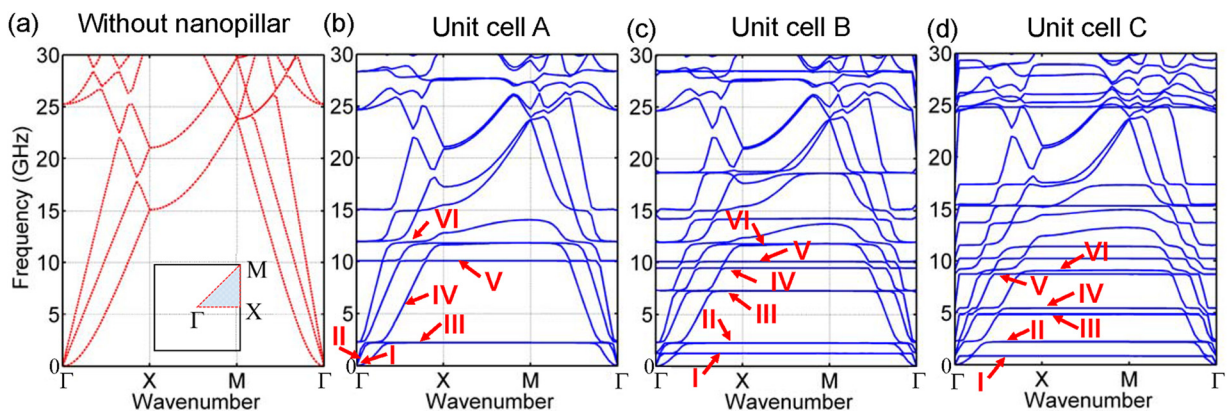


FIG. 3. Phonon dispersions for (a) the host nanomembrane, (b) hyperbranched nanomembrane consisting of unit cell A, (c) unit cell B and (d) unit cell C.

hybridization bands makes the hyperbranched NPMs a possible candidate for heat conduction tuning.

To discuss deeper physical mechanism of the hybridization bands, we snapshot several resonance modes at various representative frequencies for each unit cell. The inherent coupling and hybridization between the hyperbranched nanopillars and the host membrane are visually captured in Fig. 4. For unit cell A, the resonant modes of the flat hybridization bands are compared in Fig. 4(a). At frequencies below the hybridization bands (I, II, and IV), the entire nanostructure acts dispersionless, while around the flat bands (III, V, and VI), strong local resonances occur within the branched nanopillars. For unit cells B and C, all resonance modes are captured within the flat bands, and all of them exhibit distinct localized resonant modes in different nanopillars. The strong resonance coupling and hybridization between the nanopillars and host membrane are exhibited. Compared to the basic unit cell, the complicated hyperbranched unit cells host more phonon resonances due to the introduction of a secondary nanopillar. Figure 4(b) illustrates that additional lower- and higher-order locally resonant modes emerge by the additional branched nanopillar (I, III and IV). Furthermore, the modal shapes of the two nanopillars in unit cell B are relatively independent, because they grow on two independent surfaces. For unit cell C, we can also observe more locally resonant modes induced by the secondary branch. However, different from unit cell B, the local resonances of the two hyperbranched nanopillars in unit cell C are coupled to each other [see Fig. 4(c), II, III, and VI], which cannot be analyzed separately. Adding a secondary branch increases the tunability and practicability of the hyperbranched nanomembrane, but simultaneously increases the complexity.

B. Analytical models for hyperbranched nanostructures

To theoretically explore the flatness of the branches, the cantilever-in-mass models are proposed for various hyperbranched NPM membranes along the Γ -X direction. As shown in Figs. 1(b) and 2, the host membrane is represented by an outer mass m_1 in the cantilever-in-mass models, while the hyperbranched nanopillars are described by mass-less cantilever beams and inner masses. The effective length of the mass-less beam for the basic nanopillar is L_{e1} , and the relevant inner mass is denoted as m_2 . For unit cell B, the additional nanopillar is enacted by a separate cantilever-mass system independent from the basic nanopillar [see Fig. 2(a)]. But for unit cell C, since the secondary branch is built on the surface of the basic nanopillar, they will interact with each other during the dynamic response. We cannot separate them into two independent cantilever-mass systems during theoretical analysis. Therefore, an additional cantilever-mass system for the secondary branch is connected to the inner mass of the basic nanopillar to describe the coupling effect [see Fig. 2(b)]. The effective length of the cantilever beam and the inner mass for the additional nanopillar are L_{e2} and m_3 , respectively. Transforming these cantilever-in-mass models into classical mass-spring models, we can further obtain various lattice systems with single or dual resonators for different unit cells, as shown in Figs. 1 and 2. The mass-less cantilever beams are mimicked by a series of springs with equivalent stiffnesses k_1 or k_2 , which can be calculated based on the Euler–Bernoulli beam theory.^{34,38} For the hyperbranched nanomembrane with higher order of complexity, the corresponding equivalent lattice system can be built based on unit cells B and C [see Fig. 2(c)].

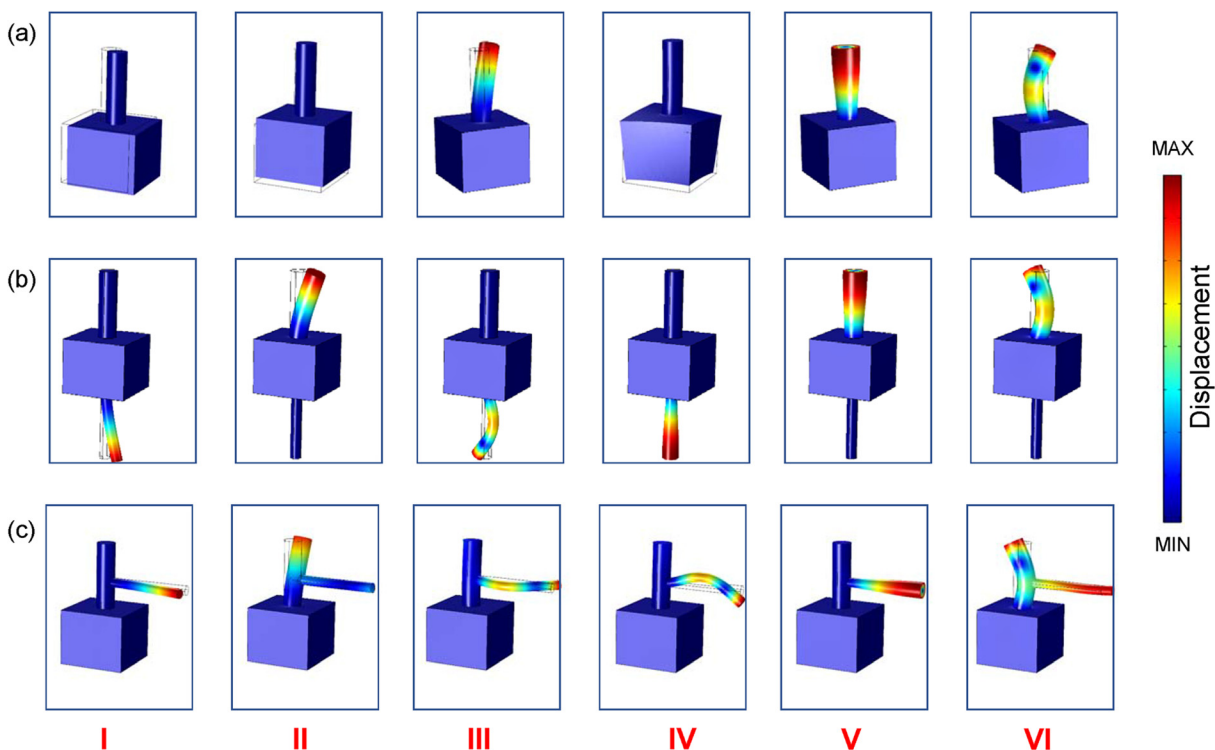


FIG. 4. Relevant resonance modes at various frequencies of I–VI for the hyperbranched NPM with (a) unit cell A, (b) unit cell B and (c) unit cell C.

For different lattice systems under a longitudinal harmonic force excitation (Γ -X direction in the hyperbranched membranes), the equations of motion are derived, respectively. as For unit cell A

$$\left. \begin{aligned} F + k_1(u_2 - u_1) - m_1 \frac{d^2 u_1}{dt^2} &= 0 \\ k_1(u_1 - u_2) - m_2 \frac{d^2 u_2}{dt^2} &= 0 \end{aligned} \right\}, \quad (1)$$

for unit cell B

$$\left. \begin{aligned} F + k_1(u_2 - u_1) + k_2(u_3 - u_1) - m_1 \frac{d^2 u_1}{dt^2} &= 0 \\ k_1(u_1 - u_2) - m_2 \frac{d^2 u_2}{dt^2} &= 0 \\ k_2(u_1 - u_3) - m_3 \frac{d^2 u_3}{dt^2} &= 0 \end{aligned} \right\}, \quad (2)$$

for unit cell C

$$\left. \begin{aligned} F + k_1(u_2 - u_1) - m_1 \frac{d^2 u_1}{dt^2} &= 0 \\ k_1(u_1 - u_2) + k_2(u_3 - u_2) - m_2 \frac{d^2 u_2}{dt^2} &= 0 \\ k_2(u_2 - u_3) - m_3 \frac{d^2 u_3}{dt^2} &= 0 \end{aligned} \right\}, \quad (3)$$

where $u_{1,2,3}$ are the displacements of $m_{1,2,3}$, respectively. For harmonic wave propagation, $F(t) = F_0 e^{-i\omega t}$ and $u_j(t) = U_j e^{-i\omega t}$, $j = 1, 2, 3$.³⁵ Then, we can obtain for unit cell A

$$\begin{bmatrix} k_1 - m_1 \omega^2 & -k_1 \\ -k_1 & k_1 - m_2 \omega^2 \end{bmatrix} \begin{bmatrix} U_1 \\ U_2 \end{bmatrix} = \begin{bmatrix} F_0 \\ 0 \end{bmatrix}, \quad (4)$$

for unit cell B

$$\begin{bmatrix} k_1 + k_2 - m_1 \omega^2 & -k_1 & -k_2 \\ -k_1 & k_1 - m_2 \omega^2 & 0 \\ -k_2 & 0 & k_2 - m_3 \omega^2 \end{bmatrix} \begin{bmatrix} U_1 \\ U_2 \\ U_3 \end{bmatrix} = \begin{bmatrix} F_0 \\ 0 \\ 0 \end{bmatrix}, \quad (5)$$

for unit cell C

$$\begin{bmatrix} k_1 - m_1 \omega^2 & -k_1 & 0 \\ -k_1 & k_1 + k_2 - m_2 \omega^2 & -k_2 \\ 0 & -k_2 & k_2 - m_3 \omega^2 \end{bmatrix} \begin{bmatrix} U_1 \\ U_2 \\ U_3 \end{bmatrix} = \begin{bmatrix} F_0 \\ 0 \\ 0 \end{bmatrix}. \quad (6)$$

Based on Eqs. (4)–(6), the following equations are derived:

$$\left. \begin{aligned} F_0 + \left(m_1 + \frac{\omega_2^2 m_2}{\omega_2^2 - \omega^2} \right) \omega^2 U_1 &= 0, & \text{for Unit cell A} \\ F_0 + \left(m_1 + \frac{\omega_2^2 m_2}{\omega_2^2 - \omega^2} + \frac{\omega_3^2 m_3}{\omega_3^2 - \omega^2} \right) \omega^2 U_1 &= 0, & \text{for Unit cell B} \\ F_0 + \left(m_1 + \frac{m_2 m_3 \omega_2^2 \omega_3^2 + m_2^2 \omega_2^2 (\omega_3^2 - \omega^2)}{m_2 (\omega_2^2 - \omega^2) (\omega_3^2 - \omega^2) - m_3 \omega_3^2 \omega^2} \right) \omega^2 U_1 &= 0, & \text{for Unit cell C} \end{aligned} \right\}, \quad (7)$$

where ω is the input frequency, and $\omega_2 = \sqrt{k_1/m_2}$ and $\omega_3 = \sqrt{k_2/m_3}$ are the localized resonance frequencies of m_2 and m_3 , respectively.

If the unit cell of a hyperbranched nanomembrane is further described by a single effective mass, and the effective masses for unit cells A, B, and C are denoted as m_{ea} , m_{eb} , and m_{ec} , respectively, based on Eq. (7), we can arrive at

$$\left. \begin{aligned} m_{ea} &= m_1 + \frac{\omega_2^2 m_2}{\omega_2^2 - \omega^2} \\ m_{eb} &= m_1 + \frac{\omega_2^2 m_2}{\omega_2^2 - \omega^2} + \frac{\omega_3^2 m_3}{\omega_3^2 - \omega^2} \\ m_{ec} &= m_1 + \frac{m_2 m_3 \omega_2^2 \omega_3^2 + m_2^2 \omega_2^2 (\omega_3^2 - \omega^2)}{m_2 (\omega_2^2 - \omega^2) (\omega_3^2 - \omega^2) - m_3 \omega_3^2 \omega^2} \end{aligned} \right\}. \quad (8)$$

The internal coupling and hybridization effects between hyperbranched nanopillars and host membrane are mathematically described in Eq. (8). Based on a single effective mass, we can describe and predict the resonance hybridization frequencies by using one equation. This equivalent approach to obtain a single effective mass is applicable for branched/hyperbranched structures with different topological complexities. The vibrational coupling effects in the hyperbranched NPMs are incorporated in the single effective mass.

Comparing various unit cells of hyperbranched nanomembrane with their relevant mass-spring models as shown in Figs. 1 and 2, we can readily obtain

$$m_1 = \rho L_p^2 L_h, \quad m_2 = \rho \pi R_1^2 L_1, \quad m_3 = \rho \pi R_2^2 L_2. \quad (9)$$

The relevant equivalent spring stiffness can be evaluated based on the Euler–Bernoulli beam theory

$$k_1 = 3EI_{x1}/L_{e1}^3, \quad k_2 = 3EI_{x1}/L_{e2}^3, \quad (10)$$

where I_x is the moment of inertia about the bending x -axis or y -axis, and for a nanopillar with a circular cross section as shown in Fig. 5(a), $I_x = \pi R^4/4$. Then, ω_2 and ω_3 are given as

$$\omega_2 = \sqrt{\frac{3ER_1^2}{4\rho L_{e1}^3 L_1}}, \quad \omega_3 = \sqrt{\frac{3ER_2^2}{4\rho L_{e2}^3 L_2}}. \quad (11)$$

The effective lengths L_{e1} and L_{e2} can be approximately estimated on the basis of dynamic analysis and continuum beam theory.^{38,39} As illustrated in Fig. 5(a), for a cantilever nanopillar with a circular cross section subjected to a load of P at the free end, we can obtain the deflection distribution along the nanopillar as

$$Y(z) = \frac{Pz^2}{6EI_x}(3L - z) = \frac{Y_{mc}}{2L^3}(3Lz^2 - z^3), \quad (12)$$

where $Y_{mc} = PL^3/(3EI_x)$ is the deflection at the free end and L is the total length of the branched nanopillar. Then, the distribution of velocity variation along the nanopillar is given by

$$V(z) = \frac{V_{mc}}{2L^3}(3Lz^2 - z^3), \quad (13)$$

where V_{mc} is the maximum velocity at the free end. Using the velocity distribution, we can calculate the maximum kinetic energy by the integral

$$\begin{aligned} K_{mc} &= \frac{1}{2} \int_0^L \rho \pi R^2 \left[\frac{V_{mc}}{2L^3}(3Lz^2 - z^3) \right]^2 dz \\ &= \frac{1}{2} \left(\frac{33}{140} \rho \pi R^2 L \right) V_{mc}^2. \end{aligned} \quad (14)$$

The branched nanopillar can also be described by another discrete system as depicted in Fig. 5(d), where the mass-less beam has the same length as the nanopillar, but the whole mass is concentrated as a tip mass of m_e at the free end. We can express the maximum kinetic energy of this equivalent system as $K_{mc} = m_e V_{mc}^2/2$. According to Eq. (14), we obtain

the equivalent tip mass as $m_e = 0.24\rho\pi R^2 L$. The resonant frequency for this discrete system is expressed as $\omega_e = \sqrt{35ER^2/(11\rho L^4)}$. Based on Eq. (11), the effective length for the hyperbranched nanopillars in the proposed cantilever-in-mass models can be further approximately estimated to

$$L_{ei} = \left[0.62/(1 - \zeta)^2 \right] L_i, \quad i = 1, 2, \quad (15)$$

where ζ is a weight factor ($0 \leq \zeta < 0.05$), which is introduced by considering the small length-to-width ratio of the nanopillars. In this case, ζ is taken to be 0.048. Then, based on Eqs. (8), (10), (11), and (15), the lower order resonance hybridization between hyperbranched nanopillars and the host membrane can be analytically analyzed. Due to less degrees of freedom, the proposed lumped mass models are not adequate to evaluate the higher order hybridization resonance modes of the hyperbranched NPMs. This is one limitation of the proposed analytical model. We can further utilize dynamic Euler–Lagrange equations to develop the analytical models for describing the high frequency flat-bands in the hyperbranched NPMs, and the relevant work about the basic branched NPMs has been discussed in the authors' previous work.²⁴

C. Hyperbranched nanopillars with various cross sections

The possible configurations and choices of cross sections of nanopillars in the literature are rather substantial.^{28,29} Here, we theoretically discuss the influence of cross section on the phonon dispersion relation. Besides the nanopillar with a circular cross section, two other types are introduced and depicted in Figs. 5(b) and 5(c), respectively. One kind is a branched nanopillar with a square cross section, and the other cross section is an equilateral triangle. The side lengths of the square and triangular cross sections are a and b , respectively. For the square and triangular nanopillars, the moments of inertia are $I_{xs} = a^4/12$ and $I_{xt} = \sqrt{3}b^4/96$, respectively. For the proposed cantilever-in-mass models, Eq. (8) is still applicable for various hyperbranched nanostructures with new cross sections, but the locally resonant frequencies of the nanopillars are modified as

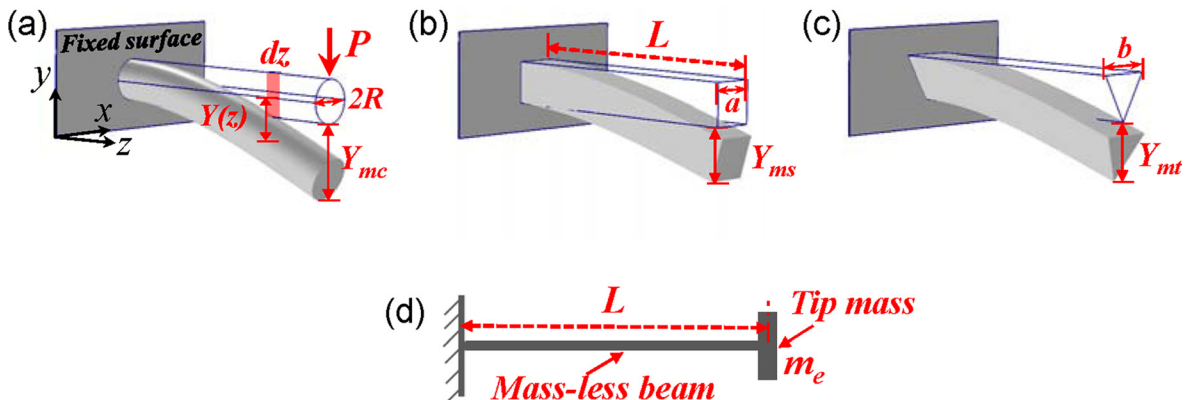


FIG. 5. Deflection distribution of a cantilever beam with (a) a circular, (b) a square and (c) an equilateral triangular cross section. (d) Sketch of a discrete beam-tip mass system.

$$\left. \begin{aligned} \omega_{2s} &= \sqrt{\frac{Ea^2}{4\rho L_{es}^3 L}}, & \text{for square cross section} \\ \omega_{2t} &= \sqrt{\frac{Eb^2}{8\rho L_{et}^3 L}}, & \text{for triangle cross section} \end{aligned} \right\}. \quad (16)$$

The maximum kinetic energy for the nanopillars containing these two cross-sections can be calculated as

$$\left. \begin{aligned} K_{ms} &= \frac{1}{2} \int_0^L \rho a^2 \left[\frac{V_{ms}}{2L^3} (3Lz^2 - z^3) \right]^2 dz = \frac{1}{2} \left(\frac{33}{140} \rho a^2 L \right) V_{ms}^2, & \text{for square} \\ K_{mt} &= \frac{\sqrt{3}}{8} \int_0^L \rho b^2 \left[\frac{V_{mt}}{2L^3} (3Lz^2 - z^3) \right]^2 dz = \frac{1}{2} \left(\frac{33\sqrt{3}}{560} \rho b^2 L \right) V_{mt}^2, & \text{for triangle} \end{aligned} \right\}. \quad (17)$$

We can further calculate the equivalent locally resonant frequencies by using the discrete system as shown in Fig. 5(d). For square cross section, $\omega_{es} = \sqrt{35Ea^2/(33\rho L^4)}$, while for triangular cross section, $\omega_{et} = \sqrt{35Eb^2/(66\rho L^4)}$. The effective lengths of the nanopillars in the proposed cantilever-in-mass model can also be evaluated for different cross sections. It is interesting that, no matter which cross section is used, the effective length can be described as $L_e = 0.62L$. Equation (15) is applicable for all branched nanopillars of various cross sections. According to Eqs. (11) and (16), for a nanopillar with a constant volume and a constant length L_1 , the resonant hybridization frequencies for circular, square and triangular cross sections can be described as

$$\begin{aligned} \omega_{2c} &= \sqrt{3Ea^2/(4\pi\rho L_{e1}^3 L_1)}, & \omega_{2s} &= \sqrt{Ea^2/(4\rho L_{e1}^3 L_1)}, \\ \omega_{2t} &= \sqrt{2Ea^2/(4\sqrt{3}\rho L_{e1}^3 L_1)}. \end{aligned} \quad (18)$$

Consequently, one can clearly see that

$$\omega_{2c} < \omega_{2s} < \omega_{2t}. \quad (19)$$

Using this equation, we can predict that the hyperbranched nanopillar with circular cross section has the lowest resonance frequency when the nanopillar volume and length are invariant, while the triangular cross section results in the highest resonance frequency.

To verify the proposed analytical models, the comparison between theoretical and numerical results is conducted for various hyperbranched nanomembranes. Based on Eqs. (8), (10), (11), and (15), we can plot the effective mass-frequency profiles for different unit cells, as shown in Figs. 6(a)–6(c). The total mass of $m_{st} = m_1 + m_2$ is utilized for normalization. The relevant phonon transmittances along the Γ -X direction (see Fig. 3) for the hyperbranched nanomembranes consisting of 10×10 unit cell A, B, or C are also numerically calculated and compared in Figs. 6(a)–6(c), respectively.

It is observed that the effective mass around the locally resonant frequencies of hyperbranched nanopillars is negative [$\omega_{2,3}$ is from Eq. (11)], while a couple of narrow bandgaps close to these frequencies is induced in the transmittance

profiles (yellow regions). The phonon transport is blocked within the bandgaps, leading to a very low phonon transmittance. The resonance hybridization frequencies can be analyzed and predicted by using the single effective mass. To distinguish the specific nanopillar by which the specific hybridization frequency is induced, we need to refer to the phonon dispersion relation and mode shapes (see Figs. 3 and 4). It is observed that due to the additional hyperbranched nanopillar, there are more bandgaps in unit cells B and C [see Figs. 6(b) and 6(c)], which enlarge the blocking influence. The additional resonant hybridization between the two coupling hyperbranched nanopillars in unit cell C modifies the phonon bandgaps slightly [see Fig. 6(c)]. For all hyperbranched nanomembranes, the numerically obtained resonances agree very well with the theoretical bands of negative mass, and also agree well with the flat hybridization bands in the phonon dispersions (see Fig. 3).

The influence of cross section on the spectral response is studied in Fig. 6(d). For hyperbranched NPM structures with the same volume and the same length but different nanopillar cross sections, the theoretical and numerical resonance frequencies are compared. For each cross section, a series of nanopillar lengths from 45 to 80 nm is selected. The theoretical resonance hybridization frequencies for each cross section can be obtained from Eq. (18). The phonon dispersion spectrums for all the configurations are numerically calculated by using COMSOL Multiphysics based on the Bloch-Floquet theory. The frequency of the first hybridization flat-band in each dispersion spectrum is captured to compare with the theoretical prediction. It is clearly exhibited in Fig. 6(d) that numerical hybridization frequencies agree very well with the theoretical analysis for all kinds of hyperbranched NPMs. In general, the resonance frequency of the first flat band decreases with an increase in the nanopillar length, which agrees with the other published results obtained by MD calculations.¹¹ As the analytical models for the resonance suggest, the nanostructure with triangular cross section always has the highest hybridization frequency, while the circular ones have the lowest values. The relevant frequencies of the square cross section are always slightly higher than the circular nanopillar. It is clearly illustrated that the inherent coupling and resonance

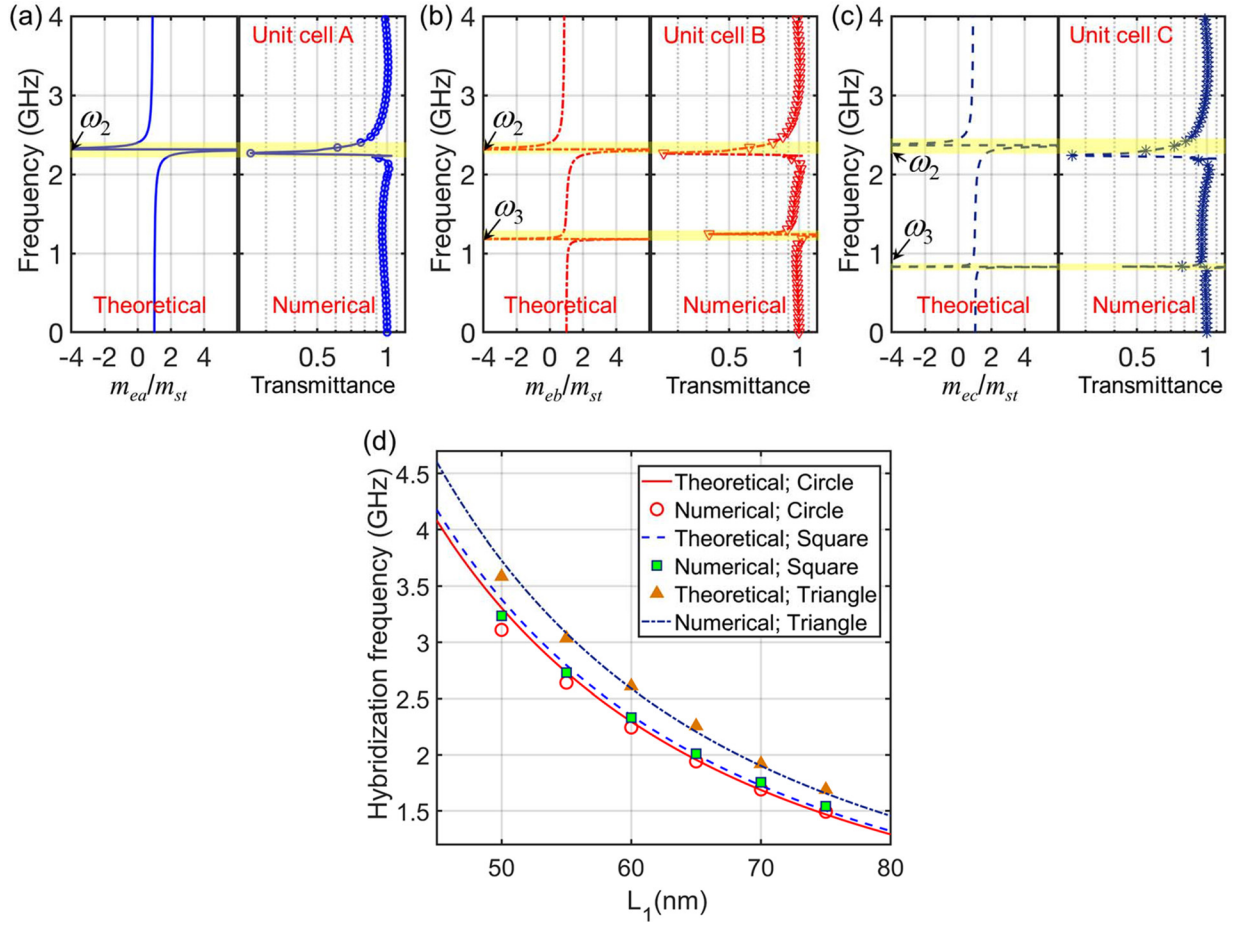


FIG. 6. Theoretical normalized mass-frequency profiles and numerical transmittance-frequency profiles for hyperbranched NMPs consisting of (a) unit cell A, (b) unit cell B and (c) unit cell C [$\omega_{2,3}$ is from Eq. (11)]. (d) Theoretical and numerical resonance hybridization frequencies obtained under different nanopillar lengths for hyperbranched NMPs with various cross-sections.

hybridization in the hyperbranched nanomembranes can be theoretically controlled and modified, which can further alter phonon group velocity and subsequently thermal conductivity. In addition, it is noticed that for the NPM with a short nanopillar (such as $L_1 = 50$ nm), the analytical results are a little higher than the numerical hybridization frequencies. It is because based on the Euler–Bernoulli beam theory,^{38,39} the cantilever-in-mass models are less suitable for thick and short nanopillars with very small length-to-width ratios. This limitation is suggested to be considered during the design of hyperbranched nanomembranes based on the proposed analytical model.

III. HEAT CONDUCTION TUNING

A. Thermal conductivity of hyperbranched nanostructures

Based on the Callaway-Holland (C-H) model,^{14,40–42} thermal conductivity of hyperbranched nanomembrane is calculated to directly illustrate how to design the heat conduction property. We can evaluate the thermal conductivity T_c by

$$T_c = \frac{1}{L_p \pi} \sum_{\gamma} \int_0^{\pi/L_e} C(\kappa, \gamma) v_g^2(\kappa, \gamma) \tau(\kappa, \gamma) \kappa^2 d\kappa, \quad (20)$$

where C is specific heat, v_g is group velocity, τ is the scattering time, and can be expressed, respectively, as

$$\left. \begin{aligned} C(\kappa, \gamma) &= k_B \left[\frac{\hbar \omega(\kappa, \gamma)}{k_B T} \right]^2 f(\kappa, \gamma) \\ v_g(\kappa, \gamma) &= \frac{\partial \omega(\kappa, \gamma)}{\partial \kappa} \\ \tau(\kappa, \gamma) &= \left[\tau_U(\kappa, \gamma)^{-1} + \tau_I(\kappa, \gamma)^{-1} + \tau_B(\kappa, \gamma)^{-1} \right]^{-1} \end{aligned} \right\}, \quad (21)$$

where κ , γ , k_B , T , \hbar , and ω are wave number, branch index, Boltzmann constant, temperature, reduced Planck's constant, and frequency, respectively. $f(\kappa, \gamma)$ can be expressed as $f(\kappa, \gamma) = e^{\hbar \omega(\kappa, \gamma)/k_B T} / [e^{\hbar \omega(\kappa, \gamma)/k_B T} - 1]^2$. τ_U , τ_I , and τ_B denote the Umklapp scattering time, impurity scattering time, and boundary scattering time, respectively, which are written as

$$\left. \begin{aligned} \tau_U(\kappa, \gamma)^{-1} &= AT \omega^2(\kappa, \gamma) e^{-B/T} \\ \tau_I(\kappa, \gamma)^{-1} &= D \omega^4(\kappa, \gamma) \\ \tau_B(\kappa, \gamma)^{-1} &= \frac{|v_g|}{L_b} \end{aligned} \right\}, \quad (22)$$

where $L_b = L_p / (1 - q)$ is the effective boundary scattering length, and $0 \leq q < 1$, which is a surface specularity

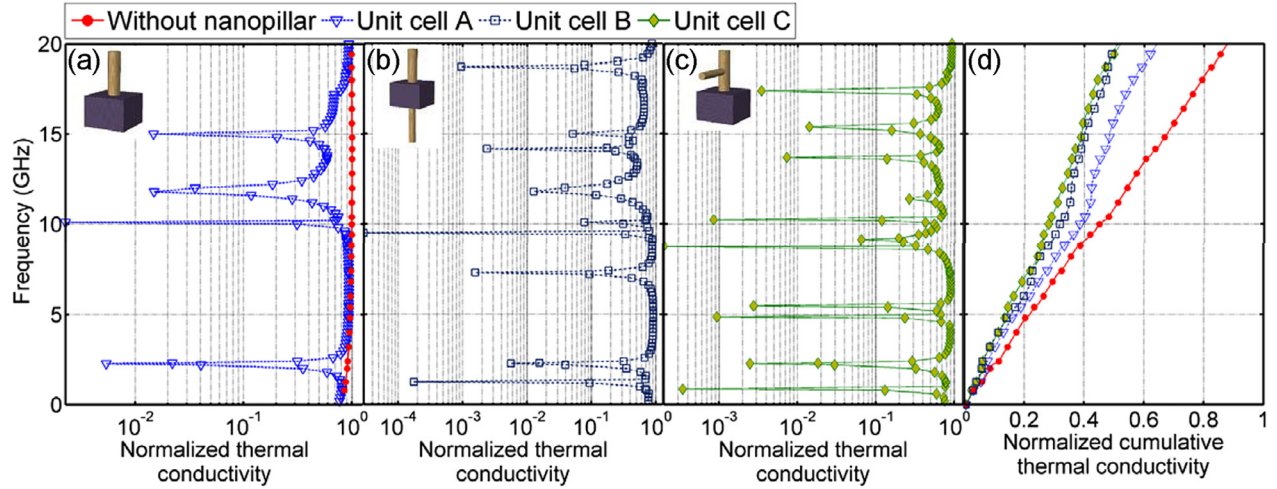


FIG. 7. Comparison of thermal conductivities as a function of frequency for (a) the host nanomembrane and the hyperbranched NPM consisting of unit cell A, (b) unit cell B and (c) unit cell C. (d) Comparison of cumulative thermal conductivities for various hyperbranched NPMs.

parameter. This thermal conductivity model mainly discusses the effect of group velocity spectrum on the heat conduction, and the dispersion dependency of heat capacity is not incorporated. In this work, we use $q = 0$, $k_B = 1.381 \times 10^{-23} \text{ JK}^{-1}$, $\hbar = 1.055 \times 10^{-34} \text{ Js}$, and $T = 0.3 \text{ K}$. The empirical coefficients A , B , and D are used as $A = 4.14 \times 10^{-15} \text{ s/K}$, $B = 899 \text{ K}$, and $D = 1.32 \times 10^{-45} \text{ s}^3$.¹⁹

According to Eqs. (20)–(22), we compute the group velocity from the dispersion relations along the Γ -X direction, and then calculate the thermal conductivity for hyperbranched nanomembranes consisting of various unit cells. In all calculations, we normalize the thermal conductivity to the unstructured host nanomembrane as shown in Figs. 7(a)–7(d). We have also calculated the thermal conductivity by using other empirical coefficients (A , B and D),⁴³ and results similar to Fig. 7 are obtained. It is observed from Fig. 7 that the nanomembranes containing nanopillars can generate a series of extraordinary low thermal-conductivity (close to zero) bands around the resonance hybridization frequencies, which agree well with the prediction frequencies by the proposed analytical models. Compared to the basic branched unit cell [Fig. 7(a)], the hyperbranched nanomembranes can generate additional ultralow thermal-conductivity bands [see Figs. 7(b) and 7(c)], which lead to more pronounced thermal conductivity reduction [see Fig. 7(d)]. Furthermore, it is observed that the normalized cumulative thermal conductivities obtained by unit cells B and C are almost identical [see Fig. 7(d)]. This is because within the same frequency range, there are similar total number of flat-bands (resonance hybridization bands) and similar total flat-band bandwidth for both configurations with two nanopillars [see Figs. 7(b) and 7(c)]. Although it has been shown from Figs. 3 and 4 that the resonance coupling effects between the two nanopillars are different for unit cells B and C, the different effects on the thermal conductivity are very slight and can be negligible, because there are only two nanopillars in these two configurations. If more branched nanopillars with different dimensions are introduced, it could be predicted that more resonance hybridization bands will be induced within a fixed

frequency range. The thermal conductivity will be altered consequently due to its strong dependency on the number of nanopillar branches. The coupling effect between nanopillars will require further research in the future. In addition, when we calculate the thermal conductivity within a higher frequency range, same conclusions can be drawn (see the Appendix). These various low thermal-conductivity bands induced by the phononic modes depend on the number, configurations and dimensions of the hyperbranched nanopillars. Finally, we can spectrally tailor these bands by using the proposed analytical models in this research, which is significantly important when designing the heat conduction behavior.

B. Thermal transport in hyperbranched nanostructures

Next, we study the thermal transports in nanomembranes with various hyperbranched nanopillars. A transient heat-transfer model for a hyperbranched nanomembrane consisting of 7×7 unit cells is built by COMSOL Multiphysics for each kind of hyperbranched NPM. As illustrated in Fig. 8(a), one end-surface of the nanomembrane is input by a heat flux with an overall heat power of $2 \times 10^{-9} \text{ W}$, while the temperature change at the opposite end surface (output surface) is recorded and compared in Fig. 8(b). A boundary condition of convective heat flux is applied to all surfaces except the heating surface. The heat transfer coefficient is $10 \text{ W}/(\text{m}^2 \text{ K})$, and the initial and external temperatures are 0.3 K . We have employed silicon-like material for thermal transport evaluation, whose thermal conductivity is $130 \text{ W}/(\text{m K})$ and heat capacity at constant pressure is $700 \text{ J}/(\text{kg K})$.

The nanomembrane without any nanopillar is taken as a reference. It should be mentioned that all kinds of hyperbranched nanomembranes have the same volume and mass to avoid the influence of different total heat capacities induced by different masses. The additional nanopillars' volume in the hyperbranched nanomembranes is homogeneously supplemented into the host nanomembrane for the

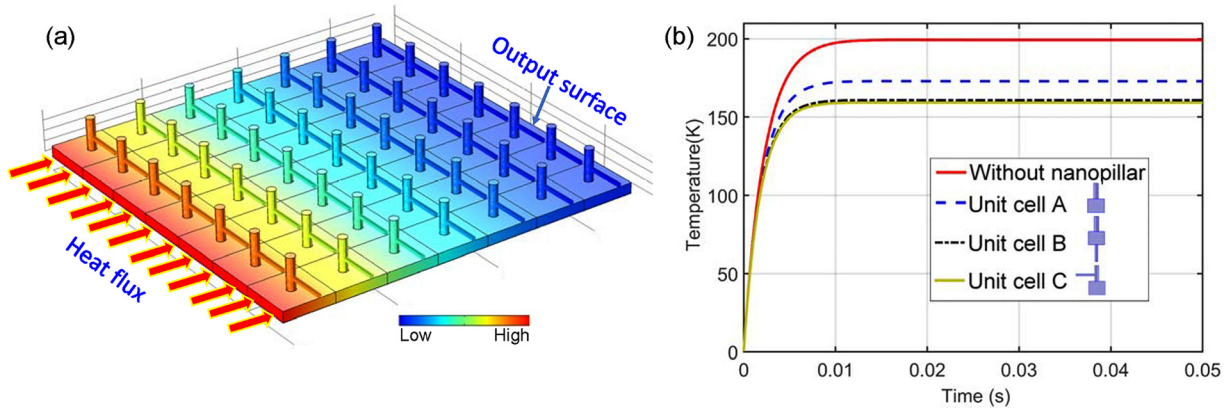


FIG. 8. (a) Temperature distribution in a transient heat flux model for a hyperbranched NPM. (b) Comparison of dynamic thermal responses in various hyperbranched NPMs.

nanostructure without or with less nanopillars to maintain the same mass for the whole structure. As depicted in Fig. 8(b), the temperature captured at the output surface has a continuous increase with time at the beginning, and then remains constant when the system reaches thermal equilibrium. It is clearly observed that under the same heating condition, the hyperbranched nanomembranes always have lower output temperature than the nanomembrane without nanopillars during the whole dynamic heat transfer process. The output temperature in the hyperbranched nanomembranes with more complexity (unit cells B and C) is significantly decreased compared to the nanomembrane that consists of the basic nanopillar (unit cell A). It is therefore proven that the hyperbranched NPMs provide more capabilities and efficiency in thermal engineering.

IV. CONCLUSIONS

In conclusion, on the basis of phonon dispersion engineering, we presented for the first time a theoretical and numerical investigation on thermal conductivity tuning in hyperbranched nanostructures. We explored the inherent coupling and resonance hybridization not only between the hyperbranched nanopillars and host membrane but also within hyperbranched nanopillars themselves. Furthermore, we constructed analytical cantilever-in-mass models to effectively analyze, optimize and control the flatness of the phonon dispersion spectrum for hyperbranched nanomembranes with various complexities and cross sections. Excellent agreement between theoretical predictions and numerical dispersion properties was obtained. It is revealed that the hyperbranched NPMs can generate many flat resonance hybridization bands, resulting in pronounced ultra-low group-velocity bands, leading to remarkable reduction in thermal conductivity. The mechanism behind the thermal conductivity reduction induced a notable superior performance in the numerical experiments on the temporal response of heat conduction. The thermal conductivity tuning in hyperbranched nanostructures can be theoretically manipulated and modified through the nanopillar designs as suggested by the proposed analytical models, which could improve future phononic and thermoelectric nanodevices.

ACKNOWLEDGMENTS

K. T. Tan acknowledges the Faculty Start-Up Grant support from The University of Akron. J.C. gratefully acknowledges financial support from the MINECO through a Ramón y Cajal grant (No. RYC-2015-17156).

APPENDIX: THERMAL CONDUCTIVITY IN EXTENDED FREQUENCY RANGE

Based on the phonon dispersions within an extended frequency range (0–50 GHz), we calculate the group velocity and obtain the thermal conductivity in a higher frequency range for various hyperbranched nanomembranes by using Eqs. (20)–(22). The normalized thermal conductivity-frequency profiles and cumulative thermal conductivity-frequency profile are exhibited in Figs. 9(a)–9(d). It is further verified that compared to the basic branched nanomembrane (unit cell A), the hyperbranched nanomembranes (unit cells B and C) can generate more extraordinary low thermal conductivity bands, leading to more thermal conductivity reduction in the extended frequency range [see Fig. 9(d)].

Furthermore, compared to the host nanomembrane without nanopillar, we calculate the reduction ratios of the cumulative thermal conductivity for the branched and hyperbranched nanostructures, as illustrated in Fig. 10. Although the reduction ratio has a relatively large change within the low frequency range (below 20 GHz), the trend converges when the frequency range is extended.

If we keep calculating the thermal conductivity for a higher frequency, inaccuracy may be induced by the uncertainty in group velocity calculation, i.e., $d\omega/d\kappa$. At a higher frequency range, there are more points where different dispersion curves seem to intersect. Normally, by using FEA solvers, it is difficult to distinguish which phonon dispersion branch these “intersection” points correspond to Ref. 23. More efforts to obtain a better evaluation of group velocities at these “intersection” points are under way.

When we reduce the dimension of the proposed hyperbranched NPMs into a similar size as that used in some molecular dynamics simulations,^{11,12,19} we obtain the phonon dispersion spectrums in THz. We plot Fig. 11 by using

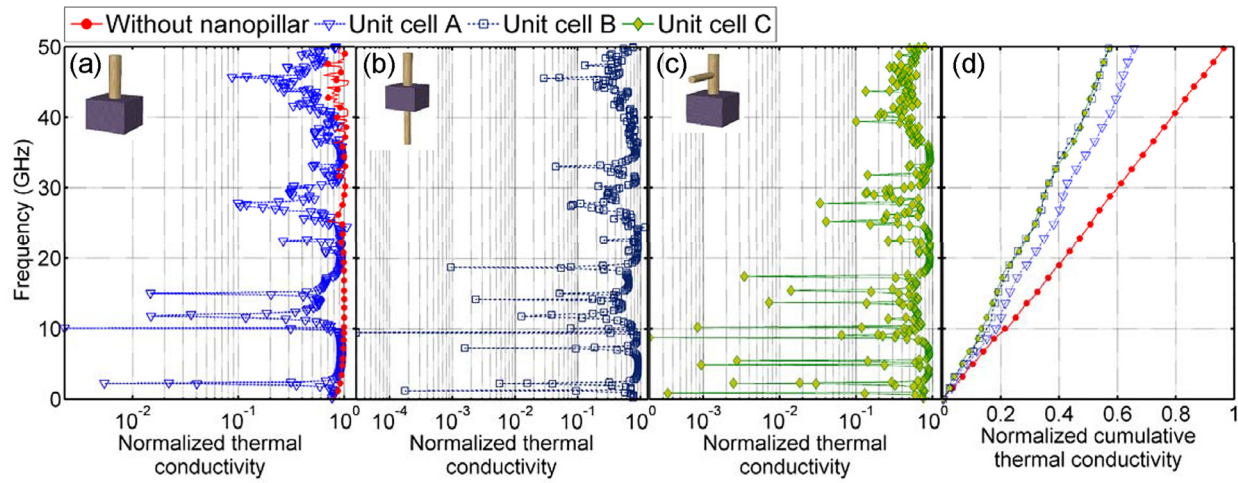


FIG. 9. Thermal conductivity-frequency profiles in extended frequency range for (a) the host nanomembrane and the hyperbranched NPMs consisting of unit cell A, (b) unit cell B and (c) unit cell C. (d) Normalized cumulative thermal conductivities in extended frequency range.

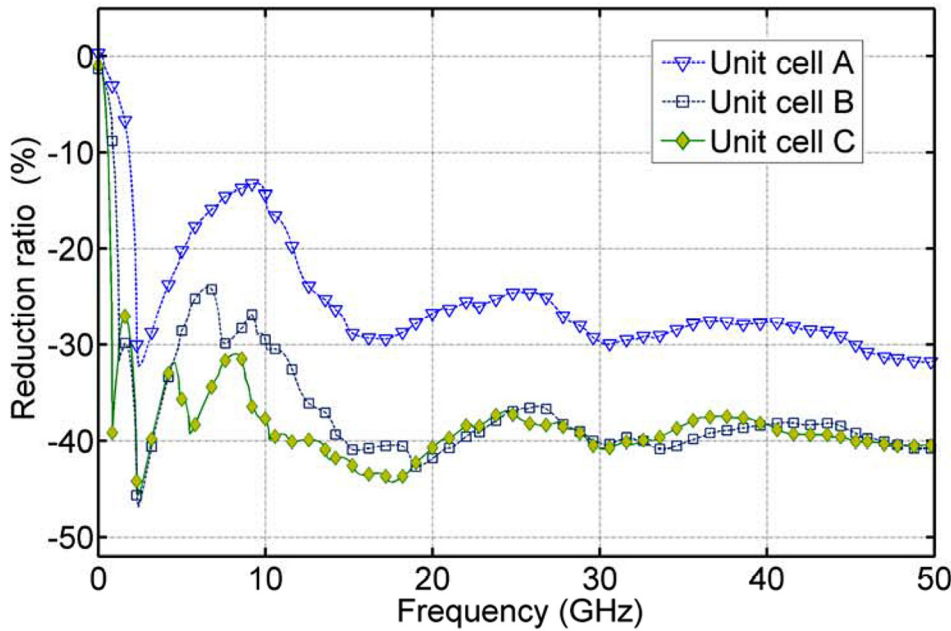


FIG. 10. Reduction ratio of the cumulative thermal conductivity as a function of frequency for various hyperbranched NPMs.

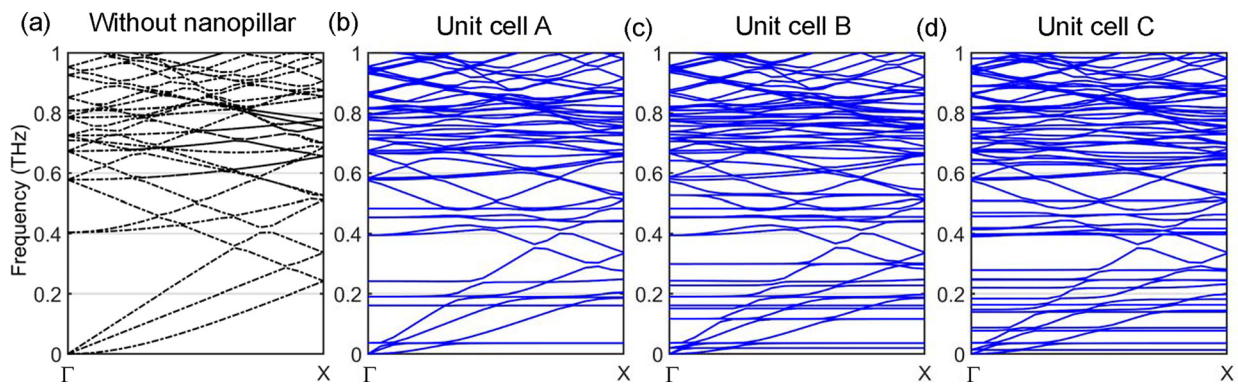


FIG. 11. Phonon dispersions obtained by small-size nanostructures for (a) the host nanomembrane, (b) hyperbranched nanomembrane consisting of unit cell A, (c) unit cell B and (d) unit cell C.

the dimension $L_p = 3.75$ nm, $L_h = 3.13$ nm, $L_1 = 3.75$ nm, $R_1 = 0.53$ nm, and for unit cell B $L_2 = 4.06$ nm, $R_2 = 3R_1/5$; for unit cell C $L_2 = 4.38$ nm, $R_2 = R_1/2$. In THz range, we also observe that compared to the host nanomembrane, the basic

branched NPM (unit cell A) can generate a series of flatbands, and the hyperbranched NPMs (unit cells B and C) can provide more resonance hybridization bands, which have more potential to realize lower thermal conductivity.

- ¹D. G. Cahill *et al.*, *Appl. Phys. Rev.* **1**(45), 011305 (2014).
- ²B. W. Li, L. Wang, and G. Casati, *Phys. Rev. Lett.* **93**(4), 184301 (2004).
- ³L. Wang and B. Li, *Phys. Rev. Lett.* **99**(4), 177208 (2007).
- ⁴Z. Q. Ye and B. Y. Cao, *Phys. Chem. Chem. Phys.* **18**, 32952 (2016).
- ⁵M. Maldovan, *Phys. Rev. Lett.* **110**(5), 025902 (2013).
- ⁶D. M. Rowe, *Thermoelectrics Handbook: Macro to Nano* (CRC Press, Boca Raton, FL, 2005).
- ⁷J. Y. Tang, H. T. Wang, D. H. Lee, M. Fardy, Z. Y. Huo, T. P. Russell, and P. D. Yang, *Nano Lett.* **10**, 4279 (2010).
- ⁸R. Anufriev and M. Nomura, *Phys. Rev. B* **93**, 045410 (2016).
- ⁹T. C. Harman, P. J. Taylor, M. P. Walsh, and B. E. LaForge, *Science* **297**, 2229 (2002).
- ¹⁰G. Pernot *et al.*, *Nat. Mater.* **9**, 491 (2010).
- ¹¹S. Y. Xiong, K. Saaskilahti, Y. A. Kosevich, H. X. Han, D. Donadio, and S. Volz, *Phys. Rev. Lett.* **117**(6), 025503 (2016).
- ¹²H. Honarvar and M. I. Hussein, *Phys. Rev. B* **93**, 081412 (2016).
- ¹³M. Maldovan, *Nature* **503**, 209 (2013).
- ¹⁴S. Alaie, D. F. Goettler, M. Su, Z. C. Leseman, C. M. Reinke, and I. El-Kady, *Nat. Commun.* **6**, 7228 (2015).
- ¹⁵J. B. Pendry, A. J. Holden, D. J. Robbins, and W. J. Stewart, *IEEE Trans. Microwave Theory Techniques* **47**, 2075 (1999).
- ¹⁶Z. Y. Liu, X. X. Zhang, Y. W. Mao, Y. Y. Zhu, Z. Y. Yang, C. T. Chan, and P. Sheng, *Science* **289**, 1734 (2000).
- ¹⁷K. Bertoldi, V. Vitelli, J. Christensen, and M. van Hecke, *Nat. Rev. Mater.* **2**, 17066 (2017).
- ¹⁸J. Christensen, M. Kadic, M. Wegener, O. Kraft, and M. Wegener, *MRS Commun.* **5**, 453 (2015).
- ¹⁹B. L. Davis and M. I. Hussein, *Phys. Rev. Lett.* **112**(5), 055505 (2014).
- ²⁰C. Kittel, *Introduction to Solid State Physics* (Wiley, New York 1976).
- ²¹H. Honarvar, L. Yang, and M. I. Hussein, *Appl. Phys. Lett.* **108**(5), 263101 (2016).
- ²²Z. Wei, J. Yang, K. Bi, and Y. Chen, *J. Appl. Phys.* **118**, 155103 (2015).
- ²³R. Anufriev and M. Nomura, *Phys. Rev. B* **95**, 155432 (2017).
- ²⁴B. Li, K. T. Tan, and J. Christensen, *Phys. Rev. B* **95**(7), 144305 (2017).
- ²⁵D. Yudistira, A. Boes, B. Graczykowski, F. Alzina, L. Y. Yeo, C. M. S. Torres, and A. Mitchell, *Phys. Rev. B* **94**(6), 094304 (2016).
- ²⁶A. Trzaskowska, S. Mielcarek, and J. Sarkar, *J. Appl. Phys.* **114**, 134304 (2013).
- ²⁷R. Anufriev, R. Yanagisawa, and M. Nomura, *Nanoscale* **9**, 15083 (2017).
- ²⁸C. W. Cheng and H. J. Fan, *Nano Today* **7**, 327 (2012).
- ²⁹H. J. Zhou and Z. R. Tian, *Prog. Nat. Sci.-Mater. Int.* **23**, 273 (2013).
- ³⁰T. R. Zhang, W. J. Dong, M. Keeter-Brewer, S. Konar, R. N. Njabon, and Z. R. Tian, *J. Am. Chem. Soc.* **128**, 10960 (2006).
- ³¹D. Wang, F. Qian, C. Yang, Z. H. Zhong, and C. M. Lieber, *Nano Lett.* **4**, 871 (2004).
- ³²G. W. Meng, Y. J. Jung, A. Y. Cao, R. Vajtai, and P. M. Ajayan, *Proc. Natl. Acad. Sci. U. S. A.* **102**, 7074 (2005).
- ³³F. H. Zhao, J. G. Zheng, X. F. Yang, X. Y. Li, J. Wang, F. L. Zhao, K. S. Wong, C. L. Liang, and M. M. Wu, *Nanoscale* **2**, 1674 (2010).
- ³⁴A. Qureshi, B. Li, and K. T. Tan, *Sci. Rep.* **6**(10), 28314 (2016).
- ³⁵B. Li, S. Alamri, and K. T. Tan, *Sci. Rep.* **7**(14), 6226 (2017).
- ³⁶P. P. Patel and P. N. Gajjar, *Phys. Lett. A* **378**, 2524 (2014).
- ³⁷A. Attaran, S. D. Emami, M. R. K. Soltanian, R. Penny, F. Behbahani, S. W. Harun, H. Ahmad, H. A. Abdul-Rashid, and M. Moghavvemi, *Plasmonics* **9**, 1303 (2014).
- ³⁸J. M. Gere and S. P. Timoshenko, *Mechanics of Materials* (PWS Publishing Company, Boston, 1997).
- ³⁹L. Meirovitch, *Analytical Methods in Vibrations* (Macmillan Publishing Co., Inc, New York, 1967).
- ⁴⁰J. Callaway, *Phys. Rev.* **113**, 1046 (1959).
- ⁴¹M. G. Holland, *Phys. Rev.* **132**, 2461 (1963).
- ⁴²B. L. Davis and M. I. Hussein, *AIP Adv.* **1**, 041701 (2011).
- ⁴³R. Y. Ma and J. R. Lukes, *J. Appl. Phys.* **123**(6), 065106 (2018).